Fibre Optic Sensing and Satellite Imaging for Early Warning of Catastrophic Ground Subsidence

Christelle Nadine Abadie, Talia Simone da Silva Burke, Sivasakthy Selvakumaran, Gianluigi Della Ragione, Yuanguo Kuang, Xiaomin Xu, Tobias Moeller, Emilio Bilotta

▶ To cite this version:

Christelle Nadine Abadie, Talia Simone da Silva Burke, Sivasakthy Selvakumaran, Gianluigi Della Ragione, Yuanguo Kuang, et al.. Fibre Optic Sensing and Satellite Imaging for Early Warning of Catastrophic Ground Subsidence. 2024. hal-04589387

HAL Id: hal-04589387
https://hal.science/hal-04589387v1

Preprint submitted on 27 May 2024

Fibre Optic Sensing and Satellite Imaging for Early Warning of Catastrophic Ground Subsidence

Christelle Nadine Abadie*
Geotechnical Centrifuge Laboratory, Department of Geotechnics, Environment, Natural Risks and Earth Sciences, Gustave Eiffel University, France
ORCID: 0000-0002-5586-6560
Email: christelle.abadie@univ-eiffel.fr

Talia Simone da Silva Burke
Department of Civil Engineering, Stellenbosch University, Stellenbosch, South Africa
ORCID: 0000-0001-9393-8601
Email: taliaburke@sun.ac.za

Sivasakthy Selvakumaran
Department of Engineering, University of Cambridge, Cambridge, UK
ORCID: 0000-0002-8591-0702
Email: ss683@cam.ac.uk

Gianluigi Della Ragione
Department of Civil, Architectural and Environmental Engineering, University of Naples, Naples, Italy
(former visiting researcher at CSIC)
ORCID: 0000-0002-2434-1438
Email: gianluigi.dellaragione@unina.it

Yuanguo Kuang
Department of Engineering, University of Cambridge, Cambridge, UK
ORCID:
Email: 2975085919@qq.com

Xiaomin Xu
Department of Solids and Structures, School of Engineering, The University of Manchester, Manchester, UK
Cambridge Centre for Smart Infrastructure and Construction (CSIC), Department of Engineering, University of Cambridge, Cambridge, UK
ORCID: 0000-0002-3185-2738
Email: xiaomin.xu@manchester.ac.uk

Tobias Möller
Department of Engineering, University of Cambridge, Cambridge, UK
ORCID:
Email: tobiasmoeller128@gmail.com

Emilio Bilotta
Department of Civil, Architectural and Environmental Engineering, University of Naples, Naples, Italy
ORCID: 0000-0002-3185-2738
Email: bilotta@unina.it

***Contact details of the corresponding author:**
Email: christelle.abadie@univ-eiffel.fr
Phone no: +33 (0) 2 40 84 56 81
Address: Université Gustave Eiffel, Campus de Nantes, Allée des ponts et chaussées - CS 5004 - 44344 Bouguenais Cedex • France

Dates text written and revised:
Paper first submitted on: 30/04/2024 to Engineering Geology
Guidelines: https://www.sciencedirect.com/journal/engineering-geology/publish/guide-for-authors
https://www.elsevier.com/researcher/author/tools-and-resources/graphical-abstract

---

Abstract (200 words)

Sinkholes pose significant risks to infrastructure and safety, emphasizing the need for early detection methods as their occurrence rises due to climate change. The ongoing SINEW project aims to provide early warning of sinkhole expansion using combined fibre optic sensing and radar satellite imaging to protect critical linear infrastructure. This paper presents key findings from experimental and numerical campaigns validating the use of distributed fibre optic sensing (DFOS) for early subsidence detection. 1*g* laboratory experiments demonstrate distinct signature strain profiles during sinkhole formation, with finite element analyses providing insight into soil-cable behaviour. Numerical scaling confirms the technique's feasibility under realistic stress levels and 3D sinkhole conditions. DFOS proves capable of detecting active sinkholes at an early stage, even when cables are situated away from the subsidence centreline, albeit a weak signal that requires complementary monitoring investigations. In this instance when uncertainty arises regarding potential cavity formation in a specific area, combined Multi-Temporal Interferometric Synthetic Aperture Radar (MT-InSAR) serves as an effective complement to pinpoint the location of the subsidence. Analysis of a car park collapse demonstrates MT-InSAR potential, detecting settlement profiles of a few millimetres years before collapse, and promising significant advancements in remote sensing technology.

Keywords (6)

Ground movements, Monitoring, Fibre optic Sensing, InSAR, Geohazards, Sinkhole

1. Introduction

Sinkhole collapses are one of the most common and disruptive geohazards. A sinkhole first develops underground with the formation of a cavity, which progressively collapses towards the surface layer. A sinkhole can also form due to the collapse of underground mines. Failure can be triggered by heavy rain, surface flooding, or pipe leakage, initiating the collapse of an otherwise stable cavity, with progressive expansion of the underground void and sagging of the upper soil layer until catastrophic collapse occurs. Ongoing climate change raises the likelihood of extreme weather, including torrential rain and flooding, and therefore sinkhole formation is becoming increasingly common.

Building on an active sinkhole presents risks of progressive ground instability, with post-collapse repairs costing from £10,000 to a few million pounds. Revealing subsidence expansion offers the opportunity for remedial work, typically grouting of the cavity (e.g. Kamal et al., 2011; Petersen et al., 2003; Qubain et al., 1995; Warner, 2004), before damage to infrastructure. However, there is, to date, no known effective method to predict active sinkholes. The technology exists, although current mature techniques (top five rows of Table 1) often require the manual and periodic monitoring of all the fissures and cavities across a large area, and/or have poor resolution.

Radar satellite-based monitoring (Interferometric Synthetic Aperture Radar, InSAR) is emerging as a powerful tool for monitoring of subsidence-induced surface settlement, with the advantage of covering extremely large areas (e.g. Baer et al., 2018; Intrieri et al., 2015; Kim et al., 2016). However, InSAR relies on the satellite's repeat-orbit cycle for its temporal frequency (typically between 4 to 35 days, see later **Table 2**), does not provide information of ground deformation at depth, and is currently computationally expensive to run without targeting a specific zone of interest. This technology might therefore be best used in conjunction with another, more frequent, localised subsurface monitoring technique. Additionally, existing studies on InSAR monitoring of sinkhole formation (e.g., Baer et al., 2018; Intrieri et al., 2015; Kim et al., 2016) primarily focus on sinkholes that emerge in inhabited regions, necessitating potentially distinct processing techniques. Further research is imperative to adapt this methodology to urban environments, where safeguarding critical infrastructures is paramount.

Table 1. Typical detection techniques for ground subsidence compared with combined DFOS and MT-InSAR (adapted from information from Moller et al. 2022, Abadie et al. 2024, Gutiérrez et al., 2019)

Technique	Temporal Frequency	Area Coverage	Resolution	Cost	Sub--surface
Seismic Wave Propagation	V. Low	V. Low	Low	High	✓
Time Domain Reflectometry	**V. High**	Medium	V. Low	Medium	✓
Ground Penetrating Radar	V. Low	Low	Low	Medium	✓
High-precision levelling	Low	V. Low	**High**	Medium	
Airborne laser scanning	V. Low	Medium	Medium	V. High	
Ground-based Interferometric Synthetic Aperture Radar	**High**	Medium	Low	Medium	
Multitemporal Interferometric Synthetic Aperture Radar (MT-InSAR)	Medium	**V. High**	Low	**Low**	
Distributed Fibre Optic Strain Sensing (DFOS)	**V. High**	Medium	**V. High**	Medium	✓

Published work on innovative methods to continuously monitor sinkhole formation below ground is limited, and the use of distributed fibre optic sensing (DFOS) has only been employed in very few field applications (Lanticq et al., 2009; Buchoud et al., 2016). There is a need to further understand this technology through systematic testing of the signature strain profile in controlled laboratory experiments (Möller et al., 2022), in the field (Guan et al. 2013; Inaudi, 2017; Xu et al., 2022b), or via numerical analyses (Linker and Klar, 2017; Della Ragione et al., 2023).

Nonetheless, active subsidence collapse affects a spatially restricted zone of a few meters to tens of meters and develops over several days, weeks or even years before sudden catastrophic failure (Baer et al., 2018). Current literature outlines that surface displacement is dominated by vertical strain (Gutiérrez et al., 2019), with sinkhole collapse generating measurable ground deformation (Chang and Hanssen, 2014). Distributed fibre optic sensing (DFOS) technologies are very sensitive to strain, can be included easily in the construction of newly built infrastructure at a limited cost, and can provide subsurface deformation measurements. This gives credence to the use of distributed fibre optic sensing for sinkhole detection.

However, is this technology able to detect sinkholes sufficiently early? Does it exhibit a clear signature strain profile that can predict the location of an active sinkhole? Are the common limitations of DFOS, such as soil-cable interface coupling, obstructing the use of the results? How can this be used in association with satellite monitoring techniques? This paper summarizes the methodology and results of the SINkhole Early Warning (SINEW) project, providing elements of responses to these questions.

1.1. The SINEW Project

The SINEW project, started in 2019, aims to identify whether the use of combined distributed fibre optic sensing (DFOS) and Multi-Temporal Interferometric Synthetic Aperture Radar (MT-InSAR) can be an efficient method to detect active sinkholes in expansion at a sufficiently early stage for ground remedial work to be actioned. These two relatively novel technologies complement each other very well for this application, as clearly shown in Table 1. Combined, they can offer a very accurate, relatively cheap method to detect sinkholes sufficiently early and over a very large area.

The project is particularly concerned with newly built linear infrastructure, such as roads or railways, for which the use of DFOS is particularly suited. The combined use of MT-InSAR enables expanded monitoring to (i) continuous detection of sinkholes when the DFOS interrogator is needed somewhere else and (ii) a larger zone, away from the linear infrastructure, facilitating the identification of sinkholes that are not forming directly below the DFOS, but still pose a potential threat to the infrastructure.

1.2. Distributed Fibre Optic Sensing

DFOS technologies - e.g., Brillouin optical time domain reflectometry (BOTDR) - use a long fibre optic cable (≥50 km), laid in the ground during earthwork or in a trench. A laser pulse is emitted by an interrogator through the fibre. Brillouin scattering infers the location and amount of axial deformation within the cable by measuring the proportional relationship between the Brillouin frequency shift of the backscatter light. This provides valuable information on soil deformation, with a spatial resolution of 0.5 to 1 m (Kechavarzi et al., 2016). Recently, developments in fibre optic sensing have permitted to improve the precision and range of measurements. Examples are Brillouin optical time domain analyser (BOTDA) and Brillouin optical frequency-domain analysis (BOFDA), which loop the cable to the interrogator and pulse a short continuous wave to the other end (Sparrevik et al., 2022), enabling a spatial resolution of a few cm, for over 50 km long cables (e.g. FibrisTerre, 2019; SMARTEC, 2010).

DFOS can also be used with different cables and interrogators to achieve even higher spatial resolution (up to 0.65 mm), but over a much-reduced distance (2.5 – 50 m) (Luna Innovations Inc., 2020). This is well adapted for laboratory experiments and provides a great opportunity to test this technology in a controlled environment to systematically understand the strain profiles obtained for specific scenarios.

1.3. Satellite Imaging

Satellite Synthetic Aperture Radar (SAR, Moreira et al., 2013) is a remote sensing technique increasingly employed in civil engineering, with applications ranging from monitoring buildings and landslides to dams. Notably, SAR offers the ability to detect small displacements in the line of sight of the sensor with a relatively high level of precision, typically achieving accuracy on the millimetre scale. While experiments in the literature have demonstrated sub-millimetre accuracy (Ferretti et al., 2007), practical use typically yields accuracy levels between 1-2 mm (Selvakumaran et al., 2020). Unlike optical-based remote sensing methods, SAR is an active system that can penetrate clouds and operate independently of weather conditions and sun illumination. An additional benefit includes the ability to historically track a region of interest if it becomes clear that deformation is occurring in an area where other monitoring instruments are not located.

The SAR system is typically mounted on a satellite platform and captures target locations in two-dimensional images. These images are acquired in two directions: the azimuth direction, corresponding to the satellite's orbit direction, and the range direction, which is perpendicular to the azimuth direction. The spatial resolution of SAR images varies among satellites, as detailed in **Table 2**. SAR-equipped satellites orbit the Earth from pole to pole, either in ascending (south to north) or descending (north to south) directions, depending on the satellite's orbit relative to Earth's rotation. This orbital pattern, combined with Earth's rotation, allows for global coverage approximately every 10-12 days. The revisit period, or the time interval between successive satellite measurements over an area of interest, determines the temporal frequency of measurements. Commercial high-resolution SAR images can be expensive; however, this study utilizes open-source data from the European Space Agency satellite constellation, Sentinel-1 (**Table 2**).

Table 2. Information about different SAR satellite options

Technique	Spatial Resolution [m x m]	Wavelength [cm]	Revisit Period	Approximate Cost/Scene [EUR]
Sentinel-1	**5 x 20**	**5.6 (C-band)**	**6 to 12 days**	**Free**
TerraSAR-X	3 x 3	3.1 (X-band)	11 days	650 – 3500
RADARSAT-2	9 x 10	5.6 (C-band)	24 days	2300 – 5000
COSMO-SkyMed	3 x 3	3.1 (X-band)	4 to 16 days	3500 – 4000
ENVISAT	4 x 20	5.6 (C-band)	35 days	1000 - 1500

Spatial resolution which determines the level of detail within images (i.e., pixel size), influences the accuracy of deformation maps and is determined by the satellite's antenna size. Wavelength, the characteristic length of radar waves emitted, varies among satellite missions operating within specific wavelengths (and frequencies). X-band and C-band frequency radars are commonly used for monitoring urban environments.

Interferometric Synthetic Aperture Radar (InSAR) techniques for deformation monitoring exploit the information contained in the phase measurement of at least two complex SAR images acquired at the same imaging geometry (ascending/descending pass direction, incidence angle, polarisation etc.) at different times over the same area, by forming an interferogram (Bamler and Hartl, 1998; Rosen et al., 2000). This deformation measurement is in the line-of-sight of the sensor. Persistent Scatterer Interferometry (PSI) relies on reflectors characterized by consistent radar responses, typically associated with robust reflecting objects, and remains stable over time. It utilizes conventional Multi-Temporal Interferometry Synthetic Aperture Radar (MT-InSAR) techniques without imposing restrictions on the temporal and spatial baselines of the multi-temporal differential interferograms utilized in the analysis (Ferretti et al.,2000, 2001). The PSI technique relies on analysing scatterers which remain coherent over a sequence of interferograms. This technique is well adapted to urban environments, which is most relevant to detecting sinkholes close to critical infrastructures in the city.

2. Modelling methods for idealised use of fibre optic sensing

For geotechnical applications, the most appropriate way to model sinkhole expansion and replicate appropriate soil stress levels would be to use a geotechnical centrifuge. However, at the time of this study, traditional DFOS analysers were not sufficiently stable to be used on the geotechnical centrifuge (Eichhorn, 2022) and this experimental method could not be used to investigate the feasibility of using DFOS for sinkhole early warning.

Consequently, a series of tests at 1*g* was first performed to systematically understand the response of DFOS cable laid over expanding subsidence in an upper cohesionless soil layer. Due to the limitations of low stress levels, the results are indicative only. The test campaign involved tests with different soil conditions (Möller et al., 2022) and cable laying techniques (Xu, et al., 2022a), rigorously analysed to identify the signature strain profile from the DFOS and its interpretation with regards to the geomechanics of the formation of a sinkhole (Möller et al., 2022). This work was successful, but weakened by uncertainties caused by the lack of coupling at the soil-cable interface at low-stress levels (1*g* experiments). To further analyse soil behaviour in the vicinity of the cable, the experimental work was supplemented with 3D finite element (FE) analyses and then scaled to realistic stress levels for applications in the field (Della Ragione et al., 2023). The present paper delves deeper into the results of both campaigns, intricately correlating and analysing how the findings from the experimental and numerical investigations underscore the efficacy of DFOS in sinkhole detection. Furthermore, it discusses how leveraging the results from this campaign could optimize the technology's performance in field applications.

2.1. Experimental Set-up

The experimental study was performed using a 790 x 200 mm rectangular rig, equipped with a trapdoor of width B = 100 mm, that can mimic the formation of a sinkhole (**Figure 1**(a)). Samples were prepared using dry Hostun sand, with an average particle size d_{50} = 0.356 mm (da Silva, 2017). The tests were prepared at increasing relative densities (D_R = 19%, 54% and 88%) to allow comparison of sinkhole formation at different soil conditions (**Table 3**). The sand was poured manually for D_R = 19% and an automatic sand pourer was used for the higher densities (Zhao et al., 2006). The sample height was H = 200 mm (H/B = 2), and one-third of the sand was dyed with dark blue ink to increase contrast for the use of Particle Image Velocimetry (PIV) to track sand particles and infer the geomechanics associated with the formation of a sinkhole. Images for the PIV analysis were acquired using two Canon Powershot G10 cameras, a ChAruCo board was used for calibration (Eichhorn et al., 2020) and the analysis was carried out using GeoPIV_RG (Stanier et al., 2016).

The trapdoor rig was actuated using a hydraulic piston. The displacement of the trapdoor, denoted as δ, was measured with the aid of two Linear Variable Differential Transformers (LVDTs) positioned beneath the trapdoor. The experiments were conducted to an ultimate displacement of δ=20 mm, corresponding to a late expansion of the sinkhole, close to collapse. Further details on the experimental set-up can be found in (da Silva, 2017; Möller et al., 2022), and the test programme used in this paper is provided in **Table 3**.

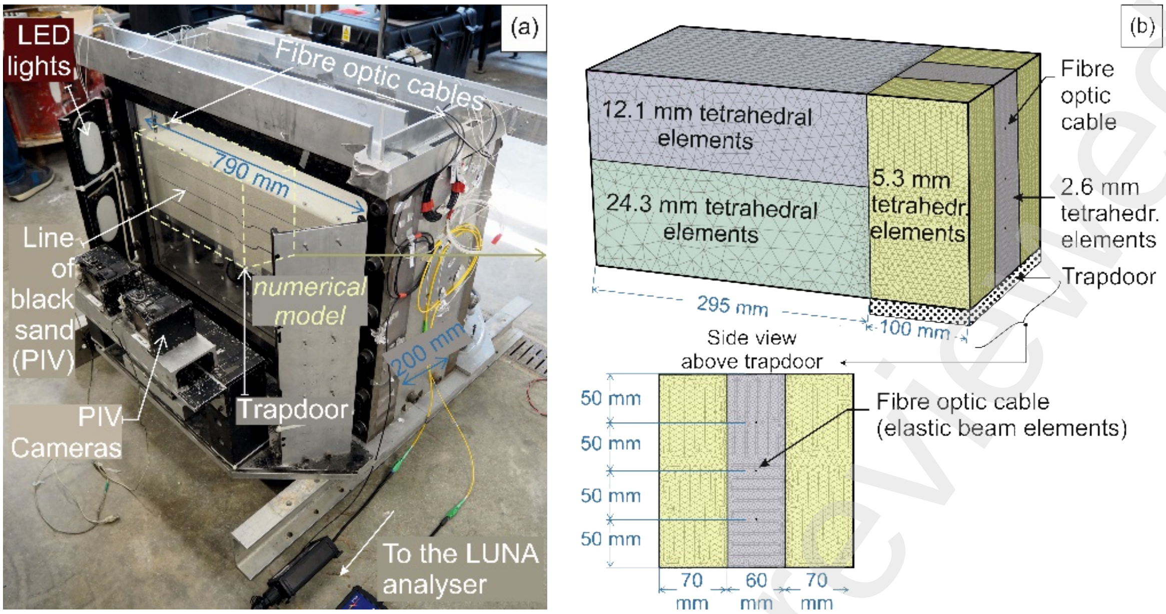

Figure 1 (a) Experimental test set-up (Exp.) and (b) replicating numerical models (Num).

Table 3. Test programme

Test	Exp. / Num.	*g* level	D_R (%)	Effect of D_R	Validate use of DFOS	DFOS strain analysis	Scale to field	Expand to 3D
E2D-19	Exp	1	19	P	P			
E2D-52	Exp	1	52	P	P	P		
E2D-88	Exp	1	88	P	P			
UNRNF-2	Exp	40	87				P	
N2D-52	Num	1	52		P	P		
N2D-R	Num	40	87		P	P	P	

Repeatability and consistency of the testing procedures were verified by repeating selected tests and comparing one test with a centrifuge test from published literature (UNRNF-2, da Silva, 2017), matching the displacement fields from the PIV and demonstrating the robustness of the testing procedure (Möller et al., 2022). UNRNF-2 was performed in the centrifuge at 40*g*, with the same experimental rig as in **Figure 1**(a), but without the use of fibre optic sensing. The relative density of the test was 87%, with a trapdoor width B = 2 m at prototype scale, and thus with the same soil height to trapdoor width H/B ratio equal to 2 used for tests E2D-19, -52 and -88 listed in **Table 3**. UNRNF-2 was also used to benchmark the numerical analyses described later in this paper

Scaling considerations

When conducting tests at 1*g*, appropriate scaling of the soil properties must be considered. In the case of sinkhole experiments, most of the geotechnical mechanism is driven by arching (da Silva, 2017),

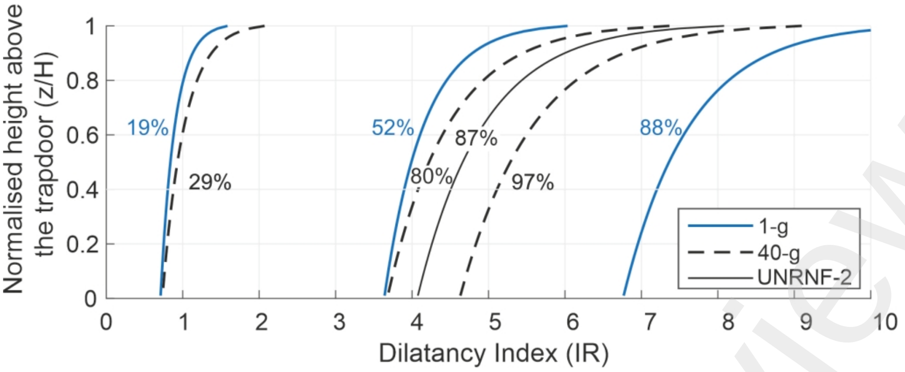

Figure 2. Comparison of relative dilatancy (I_R) for selected relative densities at 1*g* and 40*g*.

which in turn is highly dependent on soil dilation. It is hence crucial to scale the dilatancy index, I_R appropriately for 1*g* tests.

This can be achieved using the equation from (Bolton, 1986):

$$I_R = D_R \cdot (10 - \ln p') - 1 \tag{1}$$

Where p' is the effective stress. Accordingly, the tests at low relative densities limit dilation of the sample and tests at 1*g* mimic a much higher relative density in the field. This is shown in Figure 2 for tests E2D-19, -52 and -88 (at 1*g*) and UNRNF-2 (at 40*g*).

Fibre Optic Sensing

DFOS is composed of two fundamental elements: (i) the fibre optic cable to measure the strain and (ii) an optical spectrum analyser (or interrogator) to characterise the spectrum of the backscattered light and infer the axial strain within the cable.

The cable used for this study was a 2 mm diameter tight-buffed polyurethane-coated fibre optic strain sensing cable. This fibre is a common single-mode fibre (SMF) that has been widely used in structural health monitoring applications. It has a low Young’s modulus of 200 MPa and can therefore be easily pre-strained and directly integrated into loose material such as soil. Laboratory calibration tests performed at the Cambridge Centre for Smart Infrastructure and Construction (CSIC) demonstrated near-perfect strain transfer behaviour within the cable.

The DFOS cables were installed at heights of 50, 100, and 150 mm above the trapdoor, and away from the window and back edge of the box. The layers corresponding to the cable heights were highlighted using dyed black sand (see **Figure 1**(a)). The cables were laid to avoid any pre-stress and were pinned on the vertical walls of the rig. Other laying techniques were tested to improve soil-cable coupling and end effects but provided limited improvement to the results (Xu et al., 2022b).

The cables were connected to the Luna ODiSI 6100 analyser, which provides a 2.6 mm spatial resolution. The maximum measurement length for this gauge spacing is 10 m, with a sampling frequency of 25 Hz. The analyser can measure strain within a range of ±12000 με, with an error margin of ±30 με (Luna Innovations Incorporated, 2020).

2.2. Numerical Model

The numerical models implemented to further analyse the experimental results used symmetry to replicate half the geometry of the 2D 1*g* model tests (**Figure 1**(b)). A mesh consisting of 305,000 tetrahedral elements with 425,000 nodes was selected and refined around the trapdoor and the cables, where larger strains were expected.

The soil was modelled using the Hardening Soil model with small-strain stiffness (HSsmall, Benz et al., 2009; Schanz and Vermeer, 1996), which provides a balanced approach for modelling sands under low confining pressure conditions and scaled-up conditions at realistic stress levels. This method, discussed in (Della Ragione et al., 2023), offers a comprehensive representation suitable for analysing both the experimental tests and extending the work to full-scale analysis.

The fibre optic cable was modelled using an embedded beam element (Sadek and Shahrour, 2004). Meshing was implemented such that a 3-noded line element from the cable could cross a 10-noded tetrahedral element from the soil mesh. To accurately simulate the interaction between the soil and cable, a built-in interface element was employed to define the cable surface properties. Coupling at the soil-cable interface was then modelled to replicate both extreme scenarios: the optimal condition, characterized by a rough cable ($R_{inter} = 1$), and the worst-case scenario featuring a smooth cable (R_{inter}

$= 0.01$). This was achieved by defining a slippage condition on the shear force on the cable element interface t_s:

$$|t_s| = \sigma_n^{avg} \cdot R_{inter} \cdot \tan\phi' \cdot \pi \cdot D \tag{2}$$

where σ_n^{avg} is the average soil normal stress, ϕ' the mobilized angle of friction, and D the cable diameter. R_{inter} is a strength reduction factor.

The numerical analyses involved replicating the most relevant experimental test (N2D-52, Figure 2) to further understand the behaviour of the cable inside the soil body. The analysis was then scaled to realistic stress levels at 40*g* (N2D-R), replicating test UNRNF-2 and predicting what the DFOS cable response would have been.

A final analysis was performed to extend the results to the case of a 3D circular sinkhole, where cables were laid in a grid, at a distance *y* from the cable centreline (N3D-R, **Table 3**, **Figure 3**). Further information on the geometry, and mesh, and a detailed discussion of the soil and cable model is provided in (Della Ragione et al., 2023). This analysis permits extending the findings to a more realistic scenario of cavity collapse in clean fine sand to provide both expected DFOS strain profiles and surface settlement, used later in MT-InSAR analysis.

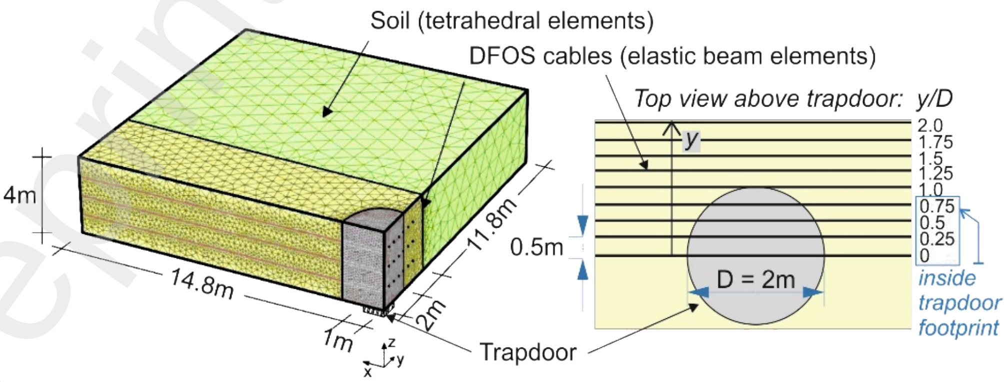

Figure 3 Cable layout in the three-dimensional numerical analysis (N3D-R)

3. DFOS for early detection of sinkhole

3.1. Results at 1g

Subsidence

PIV results were used to identify the soil behaviour and the kinematic mechanism of collapse. A modified Gaussian curve (Vorster et al., 2005) was fitted to the observed settlement profiles; the inflection point, and width of the settlement profile were determined from the fitted curve as per da Silva (2017). The results for tests E2D-19, -52 and -88 are shown in **Figure 4**. In this figure, three positions of the trapdoor were selected, corresponding to early (δ = 2 mm), medium (δ = 8 mm) and late (δ = 16 mm) formation of the sinkhole (Möller et al., 2022).

The position of the inflection points and the trough width varies as the trapdoor displacement increases, and this effect is clearer for higher relative densities. The effect of a very high relative density is indeed evident in the narrower inflection point and trough widths approaching the formation of a chimney displacement mechanism. For the lowest relative density, the inflection points remain relatively constant with height and are located along the trapdoor edge. In this diagram, the location of the DFOS cables has been highlighted using orange (bottom), yellow (middle) and blue (top) lines, and the trapdoor location in grey, a convention maintained throughout the figures of this paper. This emphasizes the anticipated deformed shape of each cable, although it remains unobservable during the experiment. The figure illustrates greater deformation with lower relative density and when the cable is positioned higher in relation to the cavity.

Influence of Relative Density

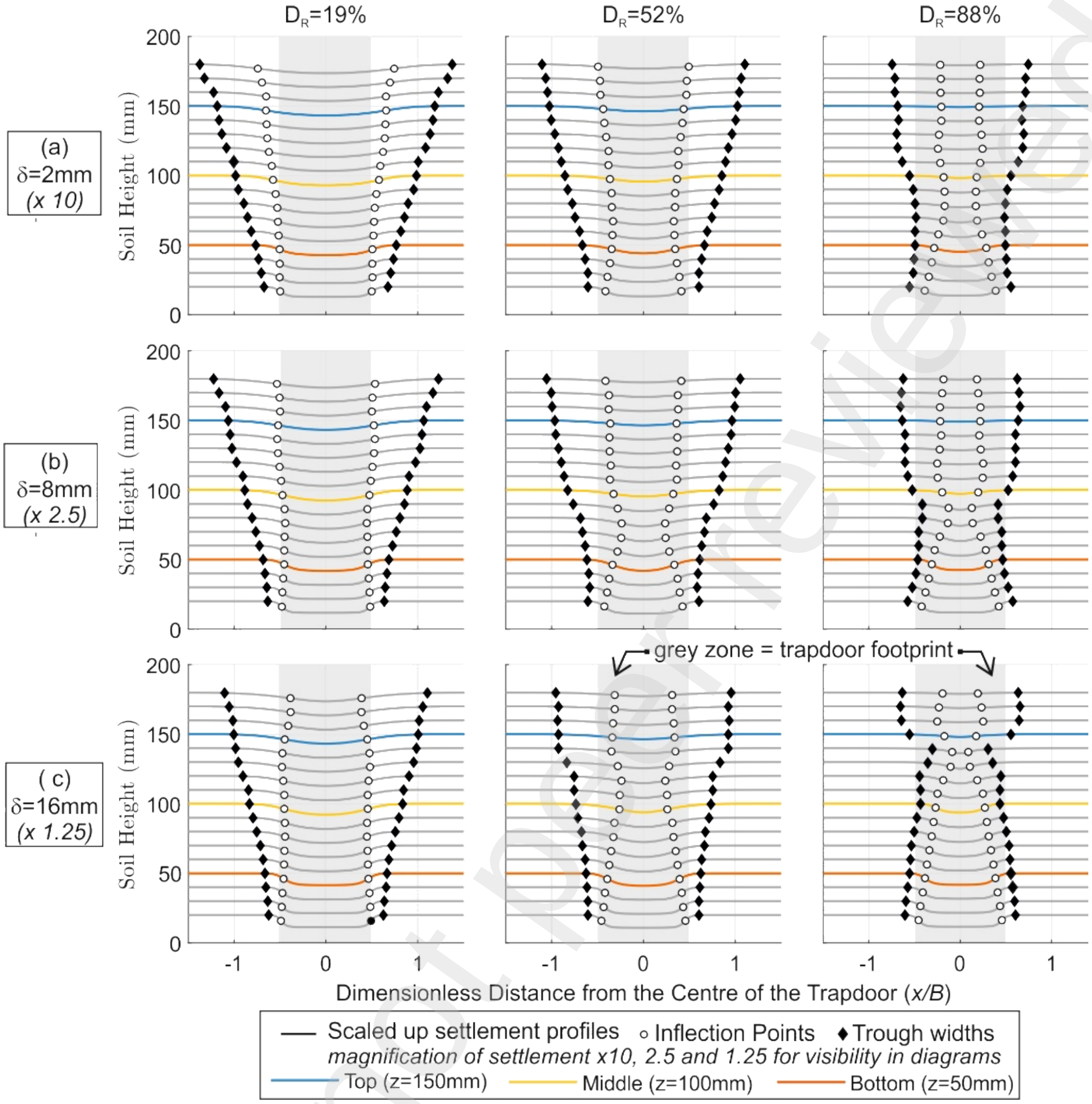

Figure 4. E2D-19, 52, 88: Inflection points position and settlement trough width derived from PIV for selected trapdoor displacement representing early (δ = 2 mm), medium (δ = 8 mm) and late (δ = 16 mm) formation of the sinkhole. Settlement profiles are magnified for clarity.

Figure 5 (a, b) display the strain recorded from PIV and a zoom of the settlement recorded at the corresponding cable depths, extracted from **Figure 4** (top row), for all three relative densities tested during the experimental campaign. A trapdoor displacement of δ = 2 mm was selected here. This aligns with the initial phase of subsidence development (Möller et al., 2022), where the onset of arching occurs following a rapid reduction in load to a minimum level, coinciding with the base movement reaching 2% of the trapdoor width, equivalent to 100 mm (da Silva Burke and Elshafie, 2021). This corresponds to the approximate point at which the signal should be detected to enable remedial work to take action.

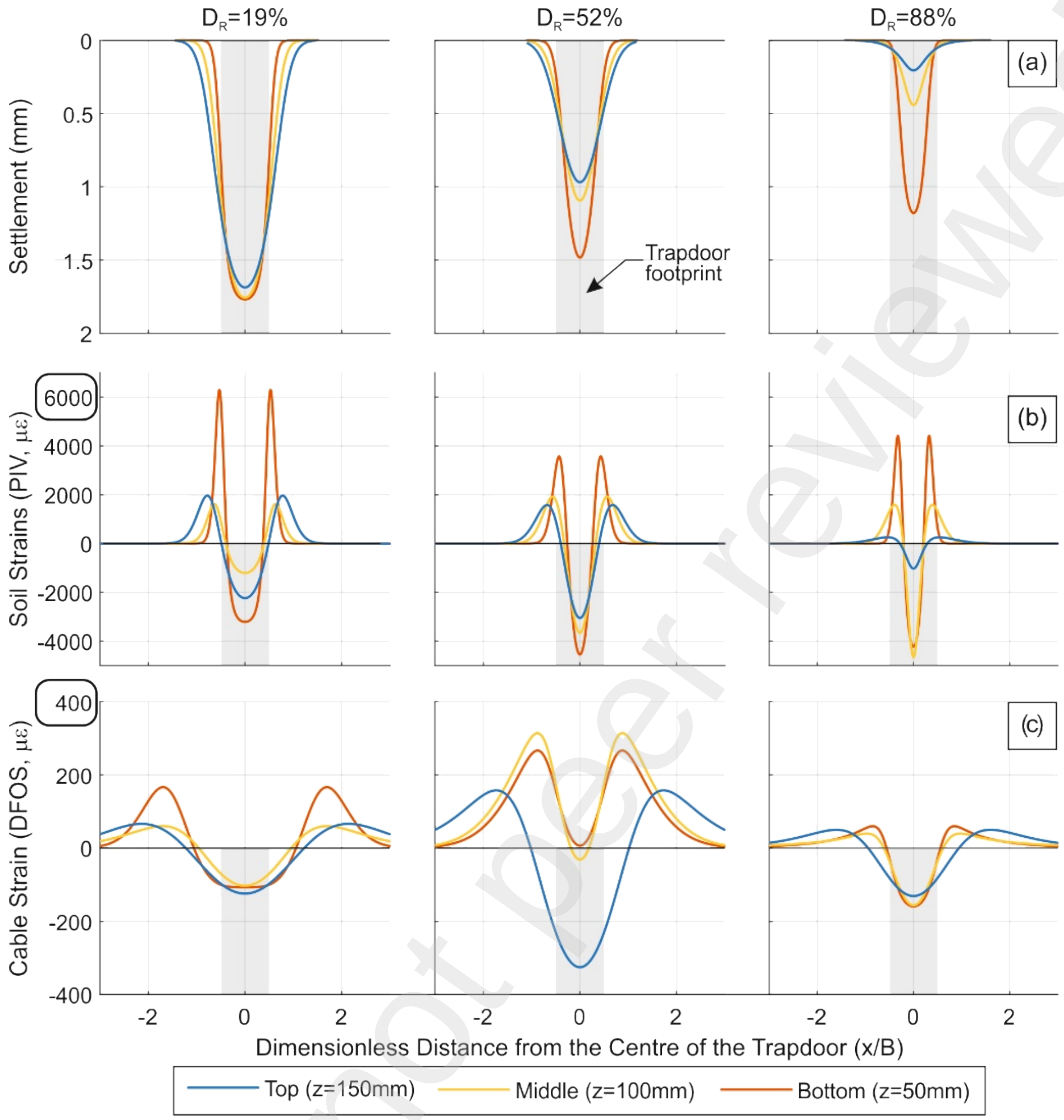

Figure 5. E2D-19, 52, 88: Profile of (a) soil settlement, (b) PIV soil strain and (c) DFOS strain at 50 mm, 100 mm and 150 mm height above trapdoor level for trapdoor displacements of 2 mm at 3 different D$_R$.

For clarity of the figures, the data from both PIV and DFOS used to derive the strain profiles throughout this paper, for both experimental and numerical data sets, were filtered and fitted using the summation of two modified Gaussian distributions following the method described in (Möller et al., 2022).

The results from **Figure 5**(a) show large settlements at low and medium relative densities, where dilation is lower, and the arching mechanism is weaker, in line with the results from **Figure 4**. The results from

PIV also show narrower strain profiles for dense soils, in line with the narrower trough widths observed in the top row of **Figure 4**. All three strain profiles display a larger strain at the bottom layer where the shear strain is the highest (da Silva, 2018; Möller et al., 2022). The differences between the middle and top layers then depend on how the funnel mechanism has developed. This is particularly evident when comparing D_R = 19% with D_R = 88%: the trough width for D_R = 19% (top left diagram of **Figure 4**) is much wider than that at D_R = 88% (top right diagram in **Figure 4**); and for D_R = 88%, the top cable is located above the arch, where not much settlement is observed (top right diagram of **Figure 5**(a)). This results in a larger and wider strain profile for the top layer of D_R = 19% than for D_R = 88%.

Fibre optic signature strain profile

The results from **Figure 5**(c) demonstrate a clear signature strain profile, with a trough located at the centre of the sinkhole, that can be used to sense the early expansion of a sinkhole. The results also prove that the DFOS cables can detect the key features of the strain profiles observed from the soil, far away from the cable, as outlined in the previous section: differences between cables and differences in the overall magnitude of the strain due to relative density.

There are, however, differences in the strain profiles that need to be explored further: (i) the magnitude of the strain in the cables is much lower compared to that experienced by the soil; (ii) the width of the strain profiles is much larger, and (iii) the strain does not return to zero at the edges of the box for low and medium dense samples.

While point (iii) can be explained from boundary effects at the edges of the box, and is a relatively minor limitation of this work, points (i) and (ii) are more prohibitive and weaken the confidence in the results shown in **Figure 5**. Point (i) is likely the product of the lack of coupling between the soil and the cable, which is largely worsened by the low-stress levels at 1*g*. Further work to understand the limitations of the soil-cable interface and its consequences at realistic stress levels is presented in Section 3.2. Point (ii) is further explored in the next paragraph.

Influence of Horizontal Ground Movement

Exploiting the high sensitivity of DFOS to small strain, **Figure 6** shows that the results obtained for a trapdoor displacement equal to 2 mm also hold for even earlier formation of the subsidence. This concurs with the results observed in the field (Xu et al., 2022b) and provides confidence in the ability of DFOS to detect sinkholes sufficiently early.

In addition, the strain from PIV was decomposed in its horizontal and vertical components to further understand the conformance of the cable strain to the ground deformation. The method to obtain this decomposition is detailed in (Möller et al., 2022).

While each profile exhibits a double peak, they diverge significantly, particularly in terms of strain magnitude. **Figure 6** demonstrates that horizontal soil displacement predominantly influences the

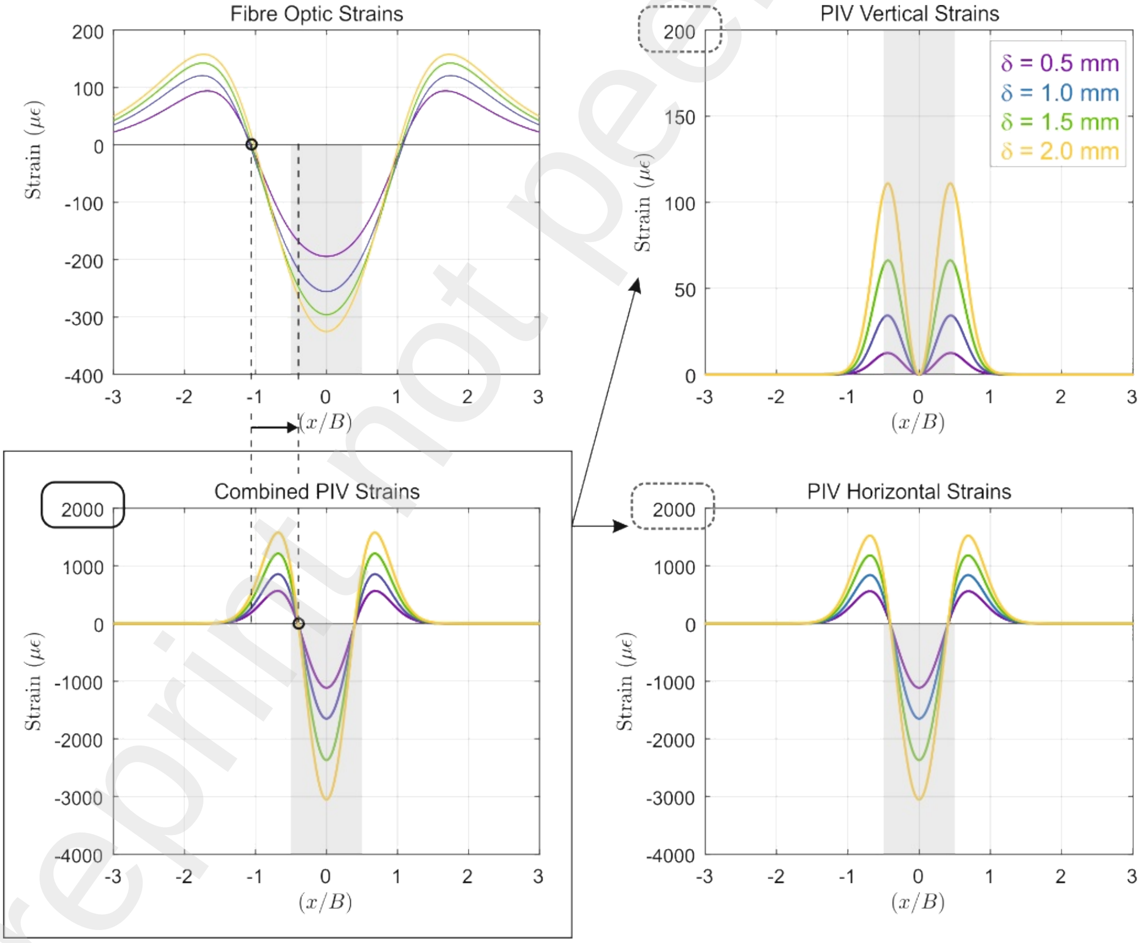

Figure 6. E2D-52: Detailed comparison between strain profiles from DFOS and PIV, with horizontal and vertical decomposition of the PIV strain for very early trapdoor displacements $D_R = 52\%, z = 150$,mm $0.5\ \text{mm} \leq \delta \leq 2.0\ \text{mm}$, top cable

combined PIV strain profile. Accordingly, the DFOS cable is measuring mostly the horizontal ground deformation. The differences observed between the DFOS strain profile and the combined PIV profile can then be explained by the cable axial stiffness, which despite being selected as low as possible (E = 200 MPa), is still much higher than that of the soil. This axial stiffness limits the longitudinal movement of the fibre when stretched, distorting the original longitudinal strain profile, and therefore the horizontal strain observed from PIV. This explains point (ii) above.

Numerical validation

The decomposition of the strain such as shown in **Figure 6** is not accessible directly from the experimental fibre optic data. To further the analysis, and elucidate point (i) and the limitations of the 1*g* tests, numerical analyses were performed, investigating both the influence of the soil-cable interface and the stress level within the soil.

The results mimicking experiments E2D-52 are shown in **Figure 7**, using the same decomposition of the strain as for **Figure 6**. First, the comparison of the total strain with experimental data, both within the soil and cable (**Figure 7**(c)), gives confidence in the numerical model, which involves the particularly challenging task of modelling soil behaviour at low-stress levels (Della Ragione et al., 2023b). Here, both the trend and magnitude of the strain are captured well. The key features observed previously in Figure 6 for the decomposition of the strain within the soil also hold in the numerical model.

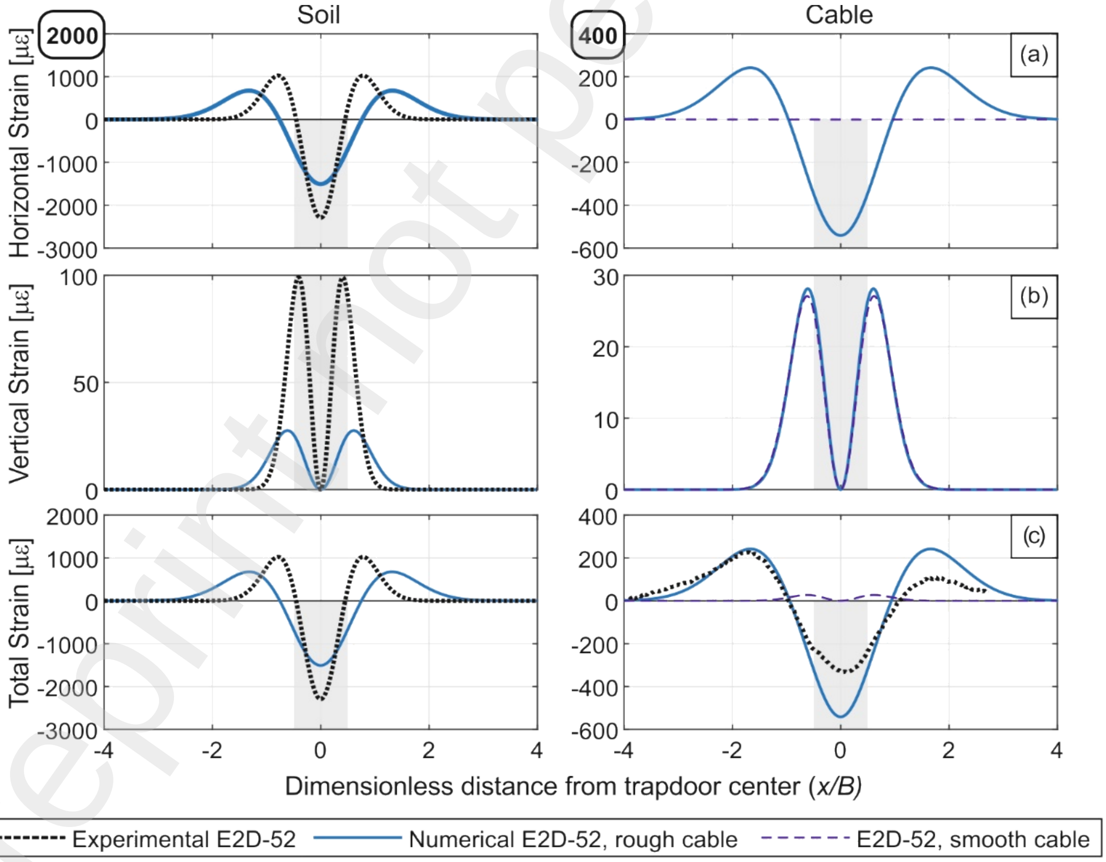

Figure 7. Analyses in 2D at 1*g* (N2D-52): Strain induced by (a) horizontal displacements; (b) vertical settlements; (c) both ground movements in (LHS) the soil and (RHS) a rough and smooth DFOS cable; compared with experimental data from E2D-52. $\delta = 2$ mm, top layer.

The contrast in strain magnitude between the cable and the soil is also observed here, which provides further confidence in the experimental techniques for the laying of the fibre optic and coupling between the soil and cable. The second column of **Figure 7** compares the case of a rough cable, fully coupled with the soil, with the case of a smooth cable. The results clearly show that the lack of coupling between the soil and the cable inhibits the cable's capacity to detect strain induced by ground horizontal movement, with the cable vertical strain conforming perfectly with the soil vertical strain. This confirms the hypothesis of Section 0, point (ii).

3.2. Applications to realistic stress levels

Figure 8 extends the findings to realistic stress levels at 40*g* for a trapdoor displacement of $\delta = 40$ mm (i.e. 2% of B), and compares the soil strain obtained from the numerical analysis to the PIV experimental data from centrifuge modelling (da Silva, 2017). The results show good agreement with the experiments, validating the model.

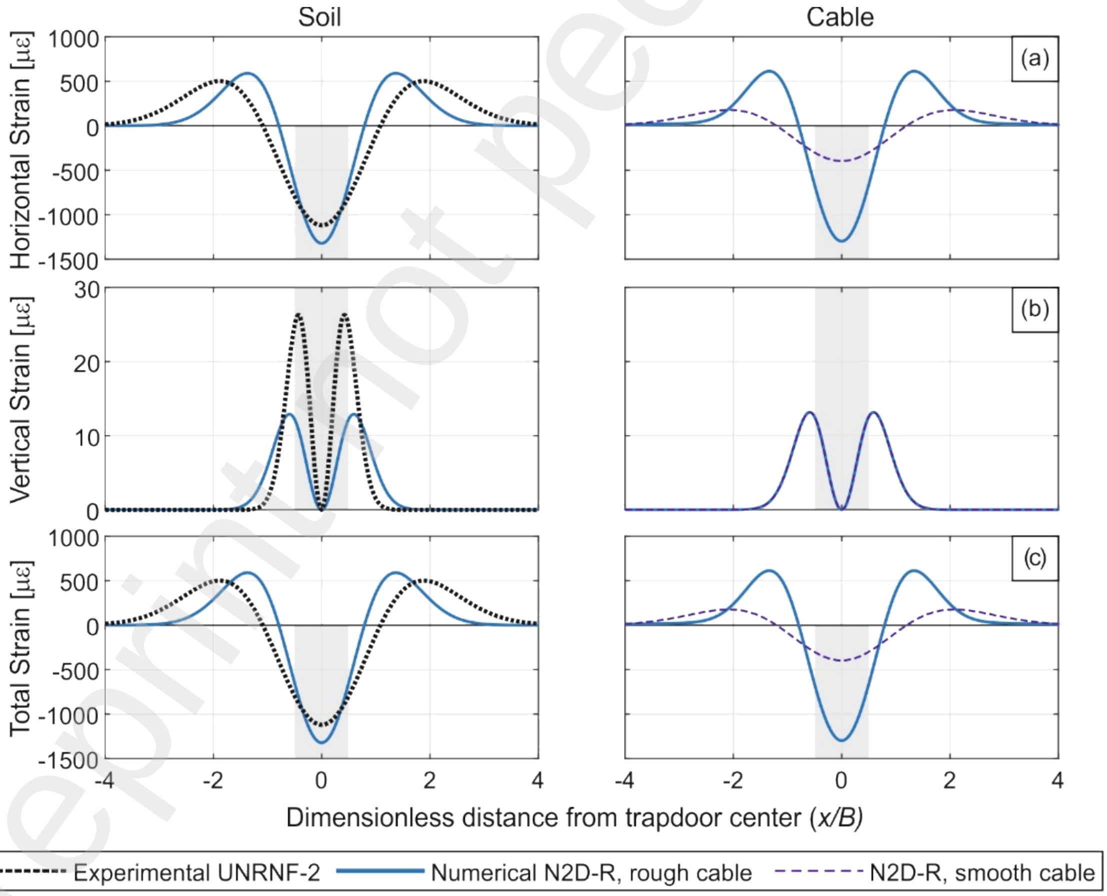

Figure 8. Analyses in 2D at 40*g* (N2D-R): Strain induced by (a) horizontal displacements; (b) vertical settlements; (c) both ground movements. (LHS) soil, compared with experimental PIV data from UNRNF-2 and (RHS from Della Ragione et al., 2023a) a rough and smooth DFOS cable. $\delta = 40$ mm, top layer

The results of **Figure 8** highlight the effect of stress level on the strain profile, and most importantly, strain magnitude of the DFOS cable (Point (i), p. 15). The results clearly show that the order of magnitude difference in strain profile disappears at realistic stress levels, highlighting the applicability of the technology for field applications but also, the key limitations of the low stress levels at 1*g* on the cable's ability to conform with soil deformation, even when improving cable laying techniques (Xu et al., 2022a).

Figure 8 also shows the expected differences between a smooth and rough cable: the lack of coupling strongly affects the strain induced by horizontal ground movements, however, not as severely as at 1*g*. Improving soil-cable coupling, for example by changing the outer shape of the cable using, for example, grip armoured cable or epsilon composite cables (Sparrevik et al., 2022), has the beneficial outcome of improving the conformity of the cable deformation with the *horizontal* soil strain. This increases the magnitude of the signature strain profile, and narrows down the width of the trough, and hence provides more accurate results on the location and extent of the sinkhole.

The results from **Figure 6**, **Figure 7** and **Figure 8** are interesting and partially concur with previous research exploring sagging subsidence, showing that the ground may experience considerable horizontal movement (Gutiérrez et al., 2012; Carbonel et al., 2014; Kim et al., 2016). However, the results from this paper show the prominence of the strain induced by horizontal movement of the ground, which had not been identified previously, and could potentially change the mindset for monitoring of sinkholes moving forward.

3.3. Extension to 3D cavity

The results from the 2D analysis at 40*g* are here extended to 3D, using the model of **Figure 3**. First, the results of the central cables, located directly above the centre of the trapdoor, with y/D = 0, are shown in **Figure 9**. The cable was modelled with a rough interface surface, capturing an ideal case scenario. Comparison of Figure 9(c) with **Figure 8** (c, RHS) shows a reduction of the strain magnitude when considering the full mechanism in 3D. Comparison of the strain profiles between the three elevations of cables shows a much narrower and stronger profile for cables located close to the trapdoor, compared with the top cable, a conclusion that concurs with the results of **Figure 5**(c) in 2D at 1*g*. The results of this graph also show good conformance of the soil strain with the cable strain, as for the 2D case.

Figure 10 finally looks at the influence of the cable location eccentricity *y/D* (see **Figure 3** for definition) by plotting the reduction in the minimum strain at the central dip (as shown in **Figure 9**) about *y/D*. The results show an abrupt reduction in strain magnitude on the edge of the trapdoor footprint ($y/D \geq 1$), which mostly affects the bottom and middle cable. The set of top cables, despite having less pronounced

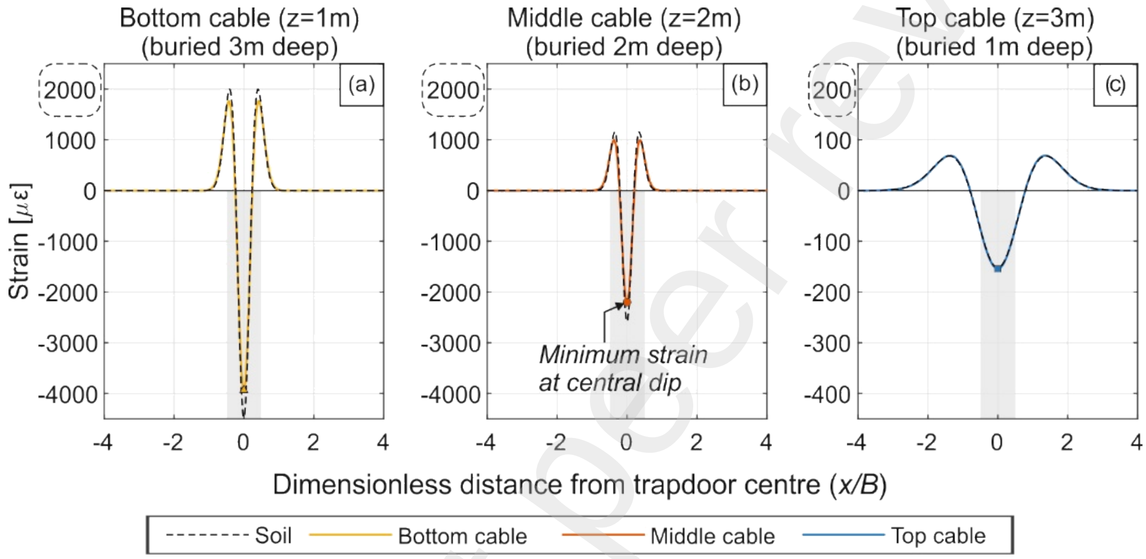

Figure 9. Analyses in 3D at 40*g* (N3D-R): Compared strain from the cable and soil obtained at the centerline of the trapdoor (*y/D* = 0, Figure 3) in the bottom, middle and top cables, $\delta = 40$ mm

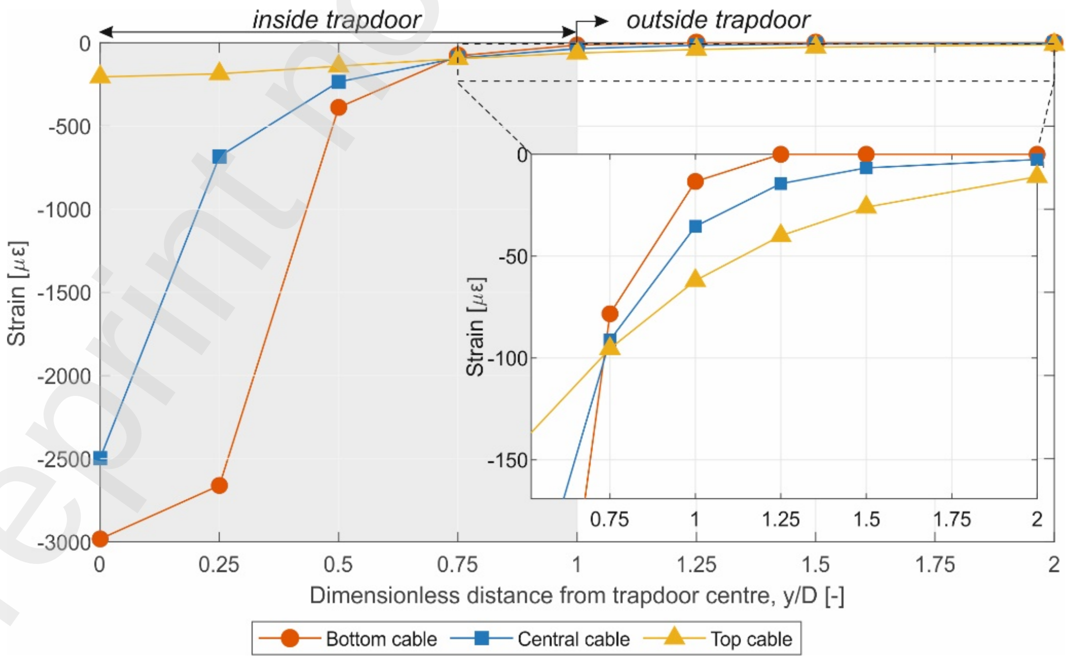

Figure 10. N3D-R: Evolution of the minimum central peak strain in DFOS cable with eccentric distance to trapdoor centerline y/D ($\delta = 40$ mm)

strain readings, is much less affected by the position of the cable with regards to the centreline, and benefits from the funnel-shape failure mechanism highlighted in **Figure 4**. The horizontal ground movement close to the surface affects a much wider zone, which the cable can sense, even when not located directly above the sinkhole footprint.

4. Satellite imaging of a real collapse

As shown in **Table 1**, the combined use of satellite and fibre optic monitoring could enhance monitoring from Distributed Fibre Optic Sensing (DFOS), in particular when the sinkhole is not forming directly below the instrumented infrastructure and the signature strain profile is weak. To explore the use of satellite monitoring in the prediction of sinkhole collapse, the collapse that occurred in the car park of the Naples Hospital on 8 January 2021 was chosen. This occurred around the time when the DFOS monitoring project was started and provided a contextual relevance to the project.

4.1. The case of Naples' hospital car park collapse

This paper targets the restricted zone of Naples' hospital car park, where a 20 m deep hole suddenly formed on the 8th of January 2021, affecting a 2,000 m^2 zone (**Figure 11**). The collapse occured following two weeks of heavy rain, engulfing a few cars and leading to the temporary closure of the Covid-19

Figure 11. Aerial Google Map view of the collapsed ground in the car park of Naples' hospital (photo credit: ANSA/AFP via Getty Images)

recovery ward. The satellite data available for this zone dates back to 2016, enabling very good tracking of the ground deformation over time.

Croce and Pellegrino (1967) and Alberico et al. (2006) report that this area mainly consists of a thin layer of remoulded fine silty sand deposit, sitting on fine silty sands, with coarse-grained sands and silty sands layers at depth. Over time, anthropic activities in the area have led to the deposition of shallow, irregular, and heterogeneous fills, potentially concealing abandoned structures from years past.

4.2. Method: Persistent Scatterer Interferometric Synthetic Aperture Radar

Persistent Scatter Interferometry (PSI) is particularly well-suited for urban areas characterized by a high density of strong radar signal reflectors such as buildings and rocks. PSI serves as an opportunistic method for measuring deformation, focusing on specific targets known as Persistent Scatters (PSs), which exhibit stability and consistent phase delivery.

Understanding coherence (also referred to as correlation) is essential as it serves as a metric of accuracy in the interferometric phase. Each pixel in the interferogram is assigned a coherence value ranging from 0 to 1. During subsequent processing, a default coherence threshold of 0.75 is typically applied, ensuring that only PSs with a correlation value exceeding 0.75 are retained.

Satellite data was acquired from Open Copernicus Access Hubs managed by the European Space Agency. SAR data, in the form of “Single Look Complex (SLC)” files, was downloaded using specific parameters outlined in **Table 4**. Only the descending data were used in this paper and proved to provide good results without the need to also process the ascending data. Adhering to these parameters ensures that the SAR images possess the necessary characteristics (such as direction and polarization) required for interferometric processing. To permit large image downloads, an automated routine leveraging the sentinelsat package can be used (Wille et al., 2017). This script automated the download process, ensuring efficient and streamlined retrieval of satellite data.

The following element of the analysis consists of establishing the Digital Elevation Model (DEM), which provides a digital representation of the Earth's topographic surface, excluding trees and buildings and

Table 4. Sentinel-1 data information for image downloads used in this paper

Sensing period	18th June 2018 to 04th of January 2021
Number of images	78
Satellite Platform	Sentinel-1A
Product type	**SLC**
Polarisation	VV
Sensor Mode	IW
Orbit Number	124
Wave band	C
Direction	Descending

is used during the processing for topographic correction. The DEM was obtained from the United States Geological Survey.

Drawing a specific area of interest (AOI) from the obtained satellite images is essential. Processing the images in their entirety would be computationally impractical. To achieve this, the most recent imagery of Naples from Google Earth can be utilized. From there, a polygon can be created to delineate the boundaries of the collapse, ensuring alignment with the actual features observed. The choice is based on a compromise between computational time and the need to be large enough to be able to adequately carry out the processing chain and correct for errors.

The acquired datasets are imported into SARSCAPE software to generate SAR images (Sarmap, 2014). To ensure data consistency, image acquisitions from different dates are carefully reviewed, with images being deselected one by one. Subsequently, the selected images undergo cropping to the Area of Interest (AOI) using a process called sample selection. This step plays a crucial role in reducing the computational load for subsequent procedures.

This enables the pre-InSAR processing, encompassing tasks like image downloading, cropping, and acquiring a Digital Elevation Model (DEM). SARscape is utilized to execute a PSI processing chain, entailing the generation of interferograms and the subsequent application of diverse corrections. These corrections include adjustments for topographic, atmospheric, and orbital errors (leveraging data from Sentinel acquisitions pertaining to precise orbit), along with noise correction.

The resulting time series can be imported into a geographic information system (GIS) like QGIS for additional analysis and interpretation. This facilitates a deeper understanding of the observed changes across the monitored area. In the subsequent section, we will present the findings of these analyses, including visual representations and interpretations of the subsidence patterns. The final output is a time-series measurement in the Line of Sight (LOS) of the satellite for each of the PS.

In this study, 78 images from the European Space Agency (ESA) Sentinel-1 C-band radar satellite from 18th June 2018 to 4th January 2021 (just before the collapse date) were processed. During interferometric processing, a digital elevation model (DEM) derived from Shuttle Radar Topography Mission (SRTM) data with a resolution of 3 arc-seconds (90 meters) was employed. The measurements noted are in the line-of-sight (LOS) of the satellite, and to estimate the vertical component of this deformation measurement, the satellite incident angle (θ, between the SAR beam and the vertical) can be used by multiplying the cosine of this angle with the line-of-sight measurement. Based on the assumption that the motion is predominantly vertical, and horizontal displacements are negligible, settlement profiles of the targeted zone are derived.

The data are processed only up to the collapse date, as there are no Persistent Scatterers (PS) available afterwards. One limitation of this technology is its inability to monitor sudden, drastic changes in the surface. However, it remains effective in monitoring surrounding infrastructure, which typically undergoes smaller, gradual changes during a collapse event. This capability has been leveraged in this study.

4.3. Satellites synchronisation

Connection diagrams illustrate the pairing of SAR images to generate differential interferograms, ensuring the reliability of the satellite imaging process. Each SAR image is multiplied by the complex conjugate of the master image to create differential interferograms. Two common representations of connection diagrams are time-position and time-baseline plots. In the PS processing method depicted in **Figure 12**, each acquisition is denoted by a diamond shape, with the yellow diamond representing the Master acquisition and green diamonds representing valid acquisitions. In this method, the Master image, dated November 5, 2019, serves as the reference image for displacement measurements. The

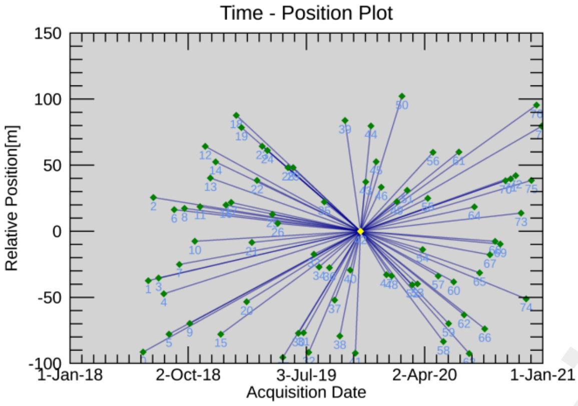

Figure 12. Time-position connection diagrams

master image was selected to ensure that the point is temporally centred and possesses a median interferogram size relative to all other points, thereby enhancing accuracy. The diagrams also indicate the distances between satellite acquisitions at different times, showing that the SAR images were captured from slightly displaced locations. Perpendicular baselines observed in the diagrams range from -200 to 50 m, within the typical range for satellite observations. However, if the separation between acquisitions exceeds 500 m, it may hinder further processing, and such pairs should be excluded from the analysis.

4.4. Evolution of ground settlement over time

The results of this analysis enable to study the ground movement of the area around Naples' hospital. **Figure 13** depicts the velocity map surrounding the collapse, generated using the PS processing method. The colour bars indicate the velocity of units in millimetres per year. Noticeably, significant subsidence is evident in the lower-left corner of the collapsed ground, likely indicating the triggering of collapse, as suggested by the high subsidence velocity. These velocity maps provide a comprehensive overview of the potential subsidence profile around the collapsed ground. Additionally, the map appears to reveal a chain of subsidence extending from the Covid-19 recovery ward to the railway, which would require further investigation.

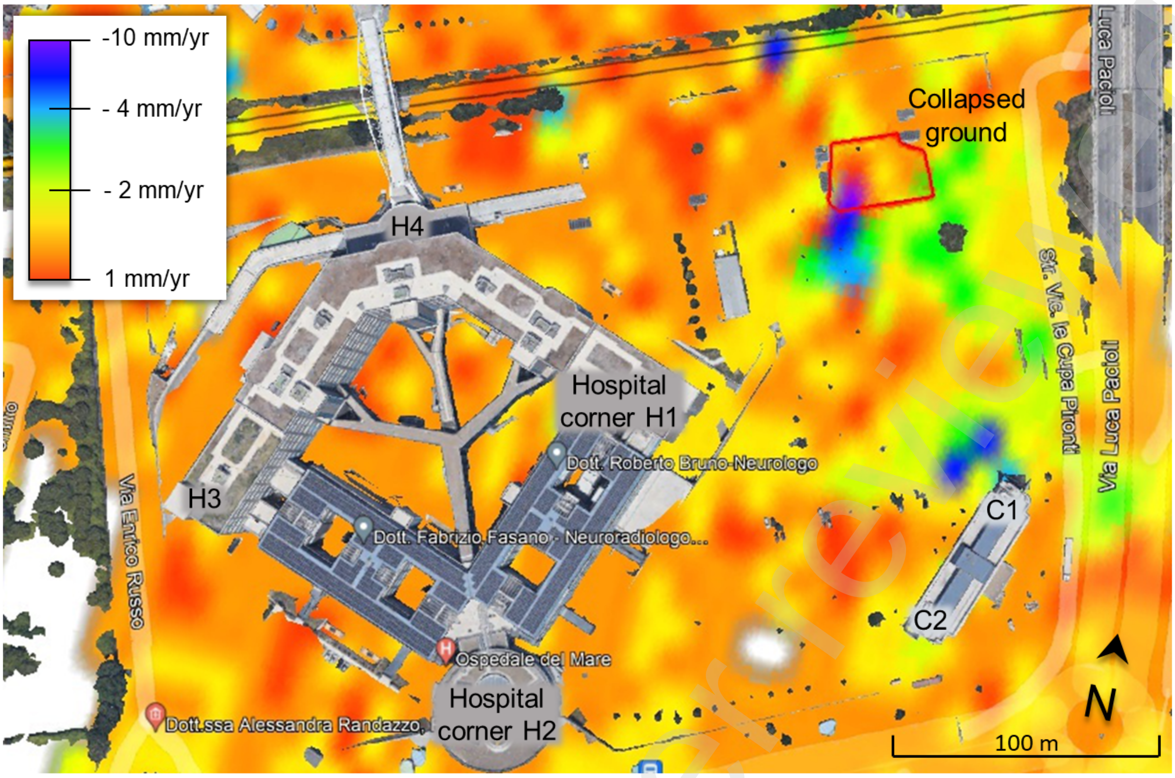

Figure 13. Vertical ground velocity map of the zone around the collapse gathering all images from June 2018 to the day before the collapse. All the time series are acquired in descending mode.

Figure 14 provides a zoomed analysis of the evolution of ground subsidence over time in the very close region surrounding the surface collapse. This figure was obtained by fitting a 3D surface to the subsidence points of measurement obtained from the satellite images in the zone immediately surrounding the area (shown in black on the graphs). The results of this set of graphs are compared with the subsidence profile of a 3D Finite Element analysis published in Della Ragione et al. (2023a,b), showing the ideal case of the early collapse of a perfectly circular cavity in clean fine sand. The images show that, quite early on, the satellite images permit evidence of a clear signature settlement profile corresponding to the formation of a subsidence at depth.

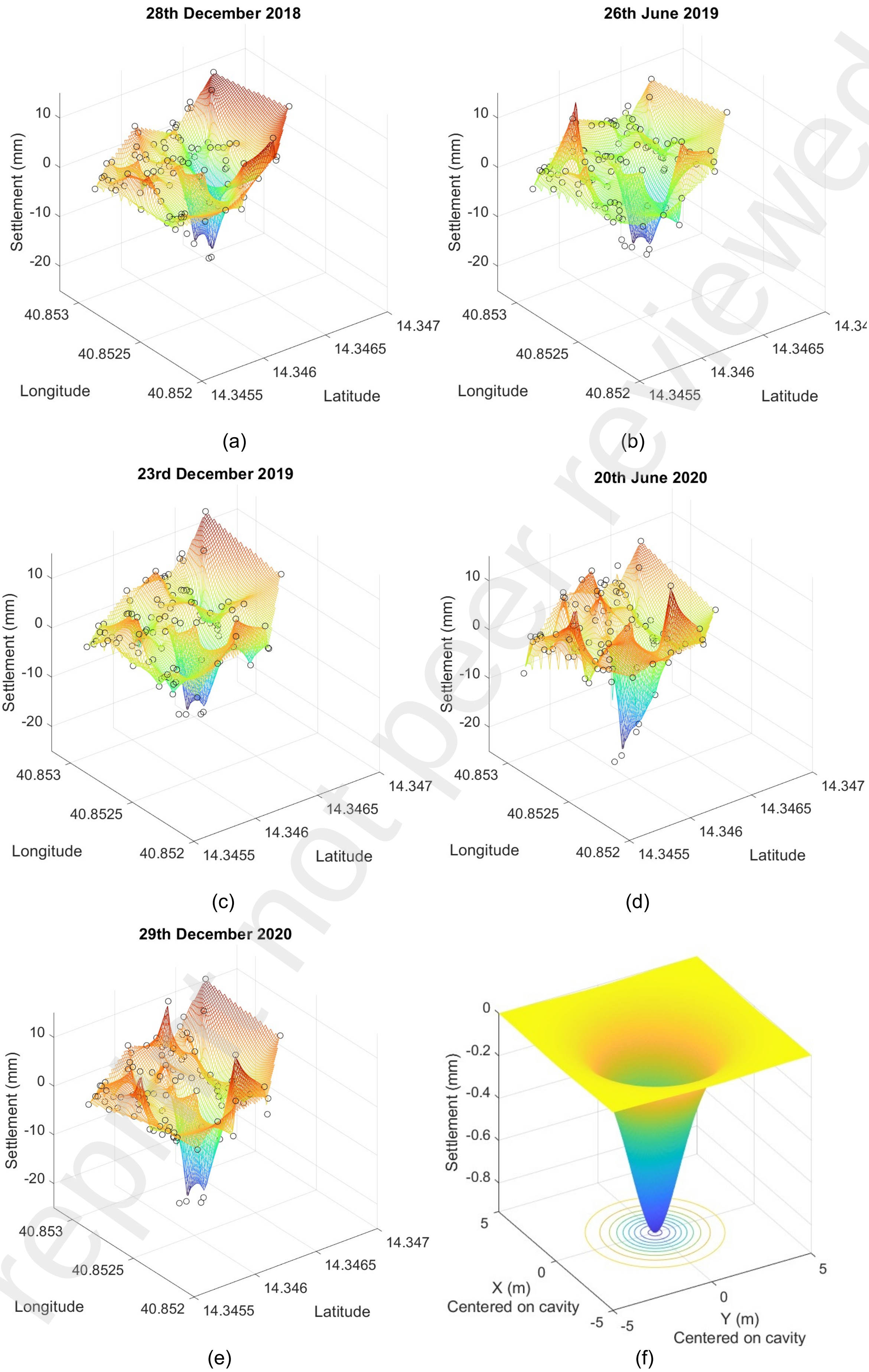

Figure 14. (a-e) Evolution of the settlement with time around the cavity before collapse (ground level is "zeroed" at the beginning of the analysis – i.e. in June 2018); (f) comparison with idealized circular cavity expansion obtained from 3D FE analysis in sand (Della Ragione et al. 2023b)

This is further analysed by taking a cross-sectional cut through selected lines along the collapsed surface damage, represented in **Figure 15** (a), and showing the evolution of the settlement profile over time, super-imposed with an estimation of an ideal sinkhole main surface damage zone.

Several observations can be drawn from the series of graphs shown in **Figure 15**(a,b c):

- **Figure 15** (b) displays a distinct subsidence profile closely resembling the ideal formation illustrated in **Figure 5** (a).
- The measured displacements are of a few millimetres, likely imperceptible to the naked eye, underscoring the resolution and capability of satellite imaging, a phenomenon noted by many in similar contexts.
- Ground subsidence appears to have been gradual, with clearly delineated profiles dating back to December 2018, nearly three years prior to collapse, highlighting the potential of remote sensing techniques for early detection.
- **Figure 15** (c) and (d) reveal that not all lines provide a clear image of subsidence evolution, warranting further research into automating monitoring processes, possibly leveraging Artificial Intelligence (AI) techniques.
- The settlement profile depicted in **Figure 15** (d) is likely influenced by the proximity of a small building (as seen in the photograph of **Figure 11**), which remains relatively stable on the periphery of the collapse. This accounts for the abrupt vertical drop observed in the settlement collapse. Similar phenomena occurred in built environment, such as the notable example of a sinkhole that emerged in Fukuoka in 2016, situated in the middle of a road flanked by towering skyscrapers. Further studies are needed to validate this observation.
- Surface damage does not necessarily correlate with the peak of subsidence observed in satellite imaging data. This is logical considering the urban setting of the studied zone: construction and ground work induce reinforcement and consolidation in some locations, which likely alter surface settlement profiles around buildings and infrastructures, diverging from the location of the cavity at depth. Consequently, detection through remote sensing techniques must be followed by specialized investigations to pinpoint the cavity before remedial action, for example, utilizing ground-penetrating radar techniques.

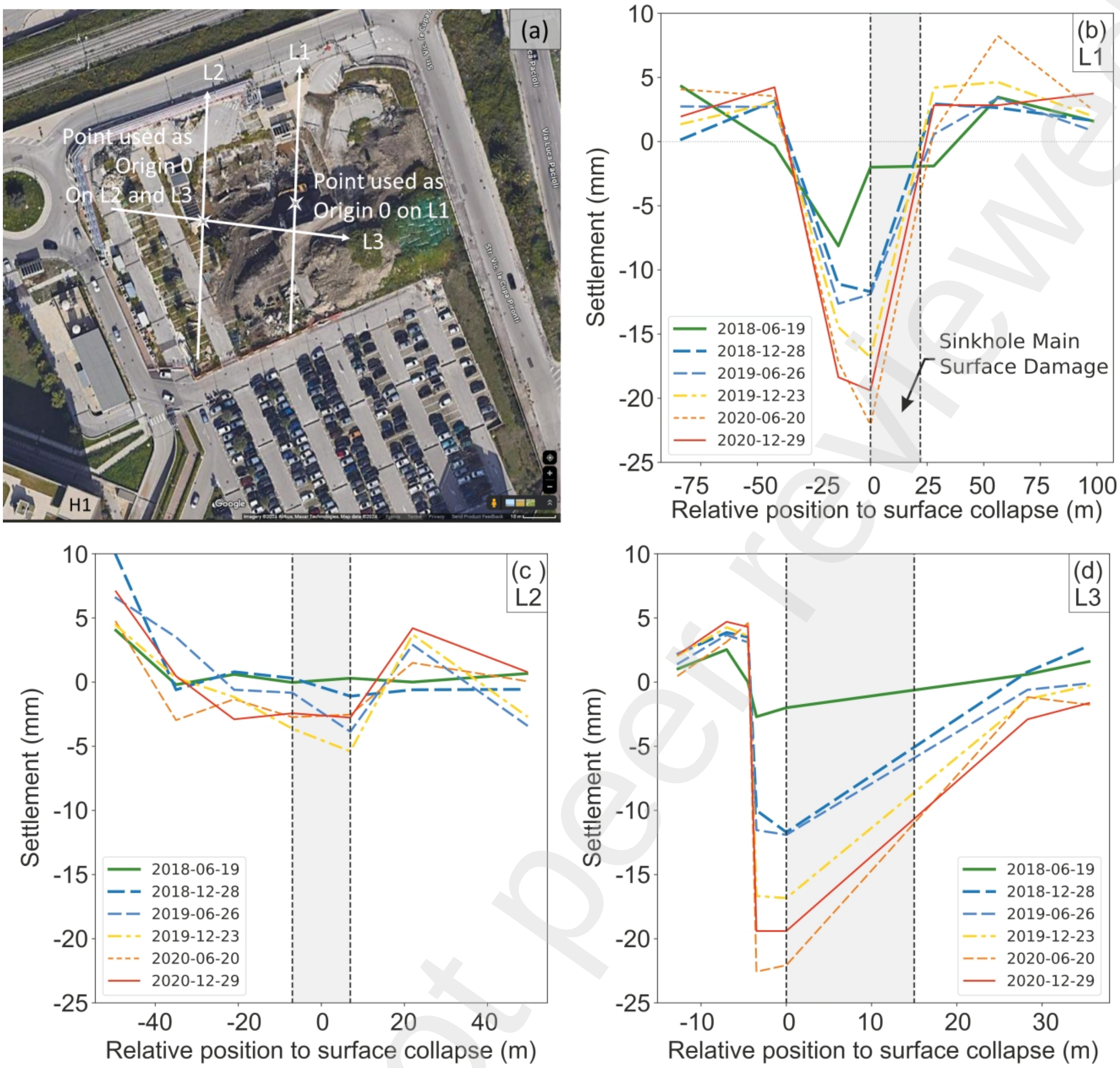

Figure 15. Evolution of cross-section settlement along selected lines with time around the cavity before collapse (ground level is "zeroed" at the beginning of the analysis – i.e. in June 2018)

4.5. Monitoring of surrounding critical infrastructure

Lastly, the satellite images used as part of the above study can also serve as a valuable tool for monitoring the evolution of surrounding infrastructure, both preceding and following the ground collapse. This technique is becoming increasingly prevalent in the surveillance of critical infrastructure, with detailed descriptions available in works such as Selvakumaran (2020), Selvakumaran et al. (2020), and Della Ragione (2024). An illustrative application is presented in **Figure 16**, which depicts the temporal vertical displacement of two hospital corners (see **Figure 13**) juxtaposed with the vertical settlement of a pertinent point within the zone later affected by collapse. In this example, the settlement was zeroed in 2018, before the occurrence of large ground subsidence (according to **Figure 15**).

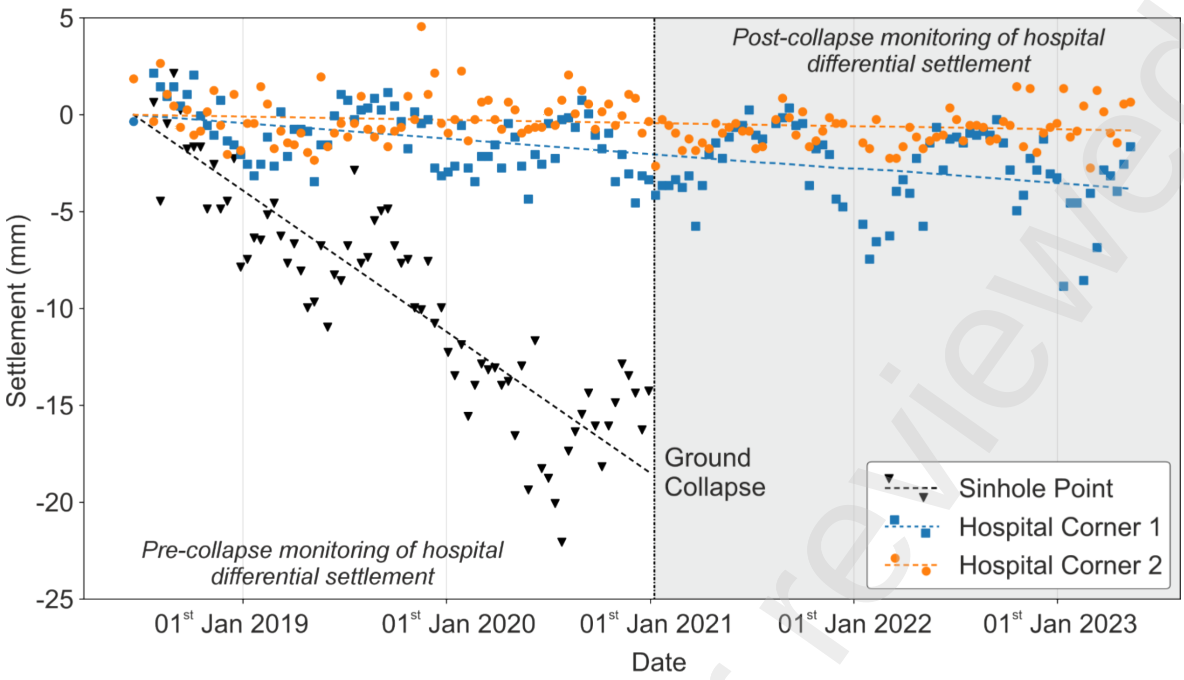

Figure 16. Evolution of the movement of selected points for monitoring of surrounding buildings: hospital and satellite building, compared with collapsed point on the ground surface

The graph exhibits seasonal changes in the building caused by swelling and contracting, which would generally be offset in a thorough analysis.

5. Conclusions

This paper, conducted as part of the SINEW (SINkhole Early Warning) project, endeavours to develop a remote sensing technique for the early detection of sinkhole collapse. Through a comprehensive approach, it demonstrates the effectiveness of leveraging Distributed Fibre Optic Sensing (DFOS) and Satellite Imaging for timely identification of sinkhole expansion. The study employs combined experimental testing at 1g and finite element analyses to validate the feasibility of DFOS, followed by a pertinent case study on a ground collapse in Naples, that well reproduces a “trapdoor” experiment at a field scale and permits to explore satellite imagery's potential and limitations.

The initial focus of the paper is on DFOS utilization. Notably, the paper highlights the prominence of the strain induced by horizontal ground movement in the combined strain response of the soil, a critical conclusion for the understanding of the DFOS response for sinkhole application. DFOS data indeed display a clear signature strain profile that captures the key features from the soil strain profile – and in particular, the strain induced by horizontal ground movement - far away from the cable. The cable strain tends to display a lower strain magnitude and a wider trough, which worsens with (i) a lower stress level and (ii) a lack of soil-cable coupling. Increasing the stress level via numerical modelling to mimic field conditions resorbed the difference in strain magnitude. In addition, enhancing soil-cable coupling clearly improves the ability of the cable to conform to soil horizontal movement and produces a clearer, narrower and stronger strain profile.

Loose cohesionless soil exhibits less dilation and therefore generates less arching at depth to support the surficial soil layer. As a result, loose and medium-dense cohesionless soil “benefit” from early higher surface settlements and larger trough width, which are easier to detect by the fibre optic. In addition, the higher the location of the cable above the sinkhole, the weaker the strain signal, but the more likely to sense the sinkhole, in particular when located far from the centreline of the subsidence. This is because cables close to the soil surface are more likely to be affected by horizontal soil movements generated by the large trough width from the funnel-shaped sinkhole mechanism close to the soil surface.

Brillouin technology is also very sensitive to small changes in material density, and as a result, the signal is easily polluted by small local changes in strain and temperature (Kechavarzi et al., 2016). Further work on the use of DFOS for sinkhole detection needs to expand the research to account for frequency shifts due to temperature, human-induced mechanical disturbances (e.g. loading, train, traffic) and vegetation growth. Additionally, the paper emphasizes the impact of cable location on signal strength and sinkhole detection, particularly when positioned away from the subsidence centreline.

In cases where DFOS signals are weak, the paper proposes the potential use of open-source data from Multitemporal Interferometry Synthetic Aperture Radar to infer soil surface settlement and velocity, aiding in narrowing down the sinkhole's position. The examination of a ground collapse that occurred in 2021 in the car park of Naples' hospital highlights that a distinct subsidence profile could have been discerned up to three years before the collapse should the technology have matured at that time. These settlement profiles are juxtaposed with idealized subsidence profiles derived from the experimental and numerical investigations conducted to validate DFOS technology, revealing promising congruence in trends for cavity collapse affecting cohesionless soil layers.

The settlement profile obtained through MT-InSAR monitoring reveals ground movements of just a few millimetres, making visual identification nearly impossible and emphasizing the necessity for high-resolution, large-area remote sensing techniques. The chosen location, nestled within a hospital car park, highlights the practicality of integrating DFOS and satellite imagery technologies in the monitoring of densely populated urban locales.

However, the study acknowledges the manual nature of its results, necessitating extensive human effort for data processing and analysis. Ongoing research aims to integrate this technology into an automated framework, leveraging Artificial Intelligence for sinkhole detection under critical infrastructure.

6. Acknowledgements

The authors thank the Cambridge Centre for Smart Infrastructure and Construction, CSIC (EPSRC (EP/N021614/1), and Innovate UK (920035)) for funding and supporting this project, as well as for facilitating collaboration between the University of Naples Federico II and the University of Cambridge, which enabled Gianluigi Della Ragione's visit to CSIC. Additionally, the authors acknowledge the Schofield Centre for their assistance with laboratory experiments. Profound appreciation is also expressed to Prof. Malcolm Bolton and Prof. Sadik Oztoprak for their insightful advice and discussions, which significantly contributed to the project's development. Special thanks are owed to Geoff Eichhorn, Dr. Alessandro Fusco, and Dr. Cedric Kechavarzi for their continuous support in the laboratory.

7. Author contribution statement (https://credit.niso.org/)

Christelle Abadie: Conceptualisation, Formal Analysis, Funding Acquisition, Methodology, Project Administration, Supervision, Writing – original draft. **Talia da Silva Burke**: Conceptualisation, Formal Analysis, Methodology, Supervision, Writing – review and editing (DFOS, Experimental and Numerical). **Sakthy Selvakumaran**: Conceptualization, Investigation, Methodology, Software, Supervision, Writing – review and editing (Satellite Imaging). **Gianluigi Della Ragione**: Data curation, Formal analysis, Investigation, Validation, Writing – review and editing (DFOS, Experimental and Numerical). **Nick Kuang**: Data curation, Formal Analysis, Investigation (Satellite Imaging). **Xiaomin Xu:** Conceptualisation, Data curation, Resources, Supervision, Writing – review and editing (DFOS, Experimental). **Tobias Möller**: Data curation, Formal Analysis (DFOS, Experimental). **Emilio Bilotta**:

Conceptualisation, Formal Analysis, Methodology, Software, Writing – review & editing (DFOS, Numerical)

8. Declaration of generative AI and AI-assisted technologies in the writing process

During the preparation of this work, the authors used Chat GPT in order to improve language and readability. After using this tool/service, the author(s) reviewed and edited the content as needed and take full responsibility for the content of the publication.

9. References

Abadie, C.N., Della Ragione, G., Kuang, N., da Silva Burke, T.S., Selvakumaran, S.,Xu, X., Moller, T., Bilotta, E. (2024) "Système de detection d'effondrement de fontis" (in French). 12èmes Journées de la Géotechnique et de la Géologie de l'Ingénieur, ENSI Poitiers, June 2024.

Alberico, I., Ramondini, M., & Zito, G. (2006) 'A database as a tool for analysis and prevention of hydrogeological instability events in an urban area: an example in the Naples area (Italy).' Italian Journal of Engineering Geology and Environment, (2), 77–92. Https://doi.org/10.4408/IJEGE.2006-02.O-05

Baer, G. Magen, Y., Nof, R. N.; Raz, E., Lyakhovsky, V., Shalev, E. (2018) 'InSAR Measurements and Viscoelastic Modeling of Sinkhole Precursory Subsidence: Implications for Sinkhole Formation, Early Warning, and Sediment Properties', Journal of Geophysical Research: Earth Surface. John Wiley & Sons, Ltd, 123(4), pp. 678–693. https://doi.org/10.1002/2017JF004594

Bamler, R. and Hartl, P. (1998) 'Synthetic Aperture Radar Interferometry.', Inverse Problems, 14.

Benz, T., Schwab, R. and Vermeer, P. (2009) 'Small-strain stiffness in geotechnical analyses', Bautechnik, 86(S1), pp. 16–27. https://doi.org/10.1002/bate.200910038

Bolton, M. D. (1986) 'Strength and dilatancy of sands', Géotechnique, 36(1), pp. 65–78. https://doi.org/10.1680/geot.1986.36.1.65

Buchoud, E., Vrabie, V., Mars, J.I., D'Urso, G., Girard, A., Blairon, S., & Henault, J. (2016). Quantification of Submillimeter Displacements by Distributed Optical Fiber Sensors. IEEE Transactions on Instrumentation and Measurement, 65(2), pp. 413–422. https://doi.org/10.1109/TIM.2015.2485340

Carbonel, D., Rodríguez, V., Gutiérrez, F., McCalpin, J.P., Linares, R., Roqué, C., Zarroca, M., Guerrero, J. and Sasowsky, I. (2014), Evaluation of trenching, ground penetrating radar (GPR) and electrical resistivity tomography (ERT) for sinkhole characterization. Earth Surf. Process. Landforms, 39: 214-227. https://doi.org/10.1002/esp.3440

Chang, L. and Hanssen, R. F. (2014) 'Detection of cavity migration and sinkhole risk using radar interferometric time series', Remote Sensing of Environment, 147, pp. 56–64. https://doi.org/10.1016/j.rse.2014.03.002

Croce, A. and Pellegrino, A. (1967). 'Il sottosuolo della Città di Napoli. Caratterizzazione geotecnica del territorio urbano'. Proceedings VIII Italian Geotechnical Conference, Cagliari, 6-7 February 1967 (in Italian).

da Silva Burke, T. S. and Elshafie, M. Z. E. B. (2021) 'Arching in granular soils: experimental observations of deformation mechanisms', Géotechnique, 71(10), pp. 866–878. https://doi.org/10.1680/jgeot.19.P.174

da Silva, T. S. (2017) Centrifuge modelling of behaviour of geosynthetic-reinforced soils above voids. PhD thesis, University of Cambridge, Cambridge, UK. Available at: https://doi.org/10.17863/CAM.21808

Della Ragione, G. (2024) An integrated approach for assessing the impact of tunnel excavations in urban areas, PhD Thesis, Univ of Napoli Federico II, Italy. http://www.fedoa.unina.it/view/subjects/

Della Ragione, G., Bilotta, E., Xu, X., da Silva Burke, T.S., Möller, T. and Abadie, C.N. (2023a) Numerical investigation of fibre-optic sensing for sinkhole detection. Géotechnique https://doi.org/10.1680/jgeot.22.00241.

Della Ragione, G., Abadie, C.N., Xu, X., da Silva Burke, T.S., Möller, T. and Bilotta, E. (2023b) Fibre optic sensing for strain-field measurement in geotechnical laboratory experiments Géotechnique Letters 2023 13:4, 196-203 https://doi.org/10.1680/jgele.23.00048

Eichhorn GN, Bowman A, Haigh SK, Stanier S. Low-cost digital image correlation and strain measurement for geotechnical applications. Strain. 2020; 56:e12348. https://doi.org/10.1111/str.12348

Eichhorn, G. N. (2022) Landslide-pipeline interaction in unsaturated silty slopes. PhD thesis, University of Cambridge.

Ferretti, A., Prati, C. and Rocca, F. (2000) 'Nonlinear subsidence rate estimation using permanent scatterers in differential SAR interferometry', IEEE Transactions on Geoscience and Remote Sensing, 38(5), pp. 2202–2212. https://doi.org/10.1109/36.868878.

Ferretti, A., Prati, C. and Rocca, F. (2001) 'Permanent scatterers in SAR interferometry', IEEE Transactions on Geoscience and Remote Sensing, 39(1), pp. 8–20. https://doi.org/10.1109/36.898661.

Ferretti, A., Savio, G., Barzaghi, R., Borghi, A., Musazzi, S., Novali, F., Prati, C. and Rocca, F. (2007). Submillimeter accuracy of insar time series: Experimental validation. IEEE Transactions on Geoscience and Remote Sensing, 45(5):1142–1153 .

FibrisTerre (2019) fTB 5020: Fiber-optic sensing system for distributed strain and temperature monitoring.

Guan, Z., Jiang, X. and Gao, M. M. (2013) 'A Calibration Test of Karst Collapse Monitoring Device by Optical Time Domain Reflectometry (BOTDR) Technique', in *13th Sinkhole Conference*.

Gutiérrez, F., Carbonel, D., Guerrero, J., McCalpin, J.P., Linares, R., Roqué, C., Zarroca, M. (2012) 'Late Holocene episodic displacement on fault scarps related to interstratal dissolution of evaporites (Teruel Neogene Graben, NE Spain)', Journal of Structural Geology, 34, pp. 2–19. https://doi.org/10.1016/j.jsg.2011.11.006

Gutiérrez, F., Benito-Calvo, A., Carbonel, D., Desir, G., Sevil, J., Guerrero, J., Martínez-Fernández, A., Karamplaglidis, T., García-Arnay, A., Fabregat, I.(2019) 'Review on sinkhole monitoring and performance of remediation measures by high-precision leveling and terrestrial laser scanner in the salt karst of the Ebro Valley, Spain', Engineering Geology, 248, pp. 283–308. https://doi.org/10.1016/j.enggeo.2018.12.004.

Inaudi, D. (2017) 'Sensing solutions for assessing the stability of levees, sinkholes and landslides', in eds ML Wang, J. L. and H. S. (ed.) Sensor Technologies for Civil Infrastructures. Woodhead Publishing, pp. 396–421.

Intrieri, E., Gigli, G., Nocentini, M., Lombardi, L., Mugnai, F., Fidolini, F., Casagli, N. (2015) 'Sinkhole monitoring and early warning: An experimental and successful GB-InSAR application', Geomorphology, 241, pp. 304–314. https://doi.org/10.1016/j.geomorph.2015.04.018.

Kamal H., El-Hawary M., Abdul-Jaleel A., Abdul-Salam S., Taha M (2011) 'Development of Cement Grout mixes for treatment of underground cavities in Kuwait', International Journal of Civil and Structural Engineering, 2(2), pp. 424–434.

Kechavarzi, C., Soga, K., de Battista, N., Pelecanos, L., Elshafie, M., Mair R. J. (2016) Distributed Fibre Optic Strain Sensing for Monitoring Civil Infrastructure. Edited by N. de Battista et al. ICE Publishing. https://doi.org/10.1680/dfossmci.60555

Kim, J.-W., Lu, Z. and Degrandpre, K. (2016) 'Ongoing Deformation of Sinkholes in Wink, Texas, Observed by Time-Series Sentinel-1A SAR Interferometry (Preliminary Results)', Remote Sensing. https://doi.org/10.3390/rs8040313

Lanticq, V.,Bourgeois, E., Magnien, P.,Dieleman, L., Gratien, V., Sang, A. Delepine-Lesoille, S. (2009) 'Soil-embedded optical fiber sensing cable interrogated by Brillouin optical time-domain reflectometry (B-OTDR) and optical frequency-domain reflectometry (OFDR) for embedded cavity detection and sinkhole warning system', Measurement Science and Technology, 20(3), p. 34018. https://doi.org/10.1088/0957-0233/20/3/034018

Linker, R. and Klar, A. (2017) 'Detection of Sinkhole Formation by Strain Profile Measurements Using BOTDR: Simulation Study', Journal of Engineering Mechanics. American Society of Civil Engineers, 143(3), p. B4015002. https://doi.org/10.1061/(ASCE)EM.1943-7889.0000963

Luna Innovations Incorporated (2020) 'Optical Distributed Sensor Interrogator Model ODiSI 6100: Data Sheet'. Blacksburg, VA, USA.

Möller, T., da Silva-Burke, T.S., Xu, X., Della Ragione, G., Bilotta, E., Abadie, C.N. (2022) 'Distributed fibre optic sensing for sinkhole early warning: experimental study', Géotechnique, 0(0), pp. 1–15. https://doi.org/10.1680/jgeot.21.00154

Moreira, A., Prats-Iraola, P., Younis, M., Krieger, G., Hajnsek, I., Papathanassiou, K.P. (2013). A tutorial on synthetic aperture radar. IEEE Geoscience and remote sensing magazine, 1(1):6–43. https://doi.org/10.1109/MGRS.2013.2248301

Petersen, W. K., Meyers, J. R. and Mackey, R. R. (2003) 'Sinkhole remediation measures for a highway in King of Prussia, Pennsylvania', in Geotechnical Special Publication, pp. 569–579. https://doi.org/10.1061/40698(2003)52

QGIS Development Team. QGIS Geographic Information System. QGIS Association

Qubain, B. S., Seksinsky, E. J. and Aldin, E. G. (1995) 'Techniques to investigate and remedy sinkholes', Karst geohazards: engineering and environmental problems in karst terrane. Proc. 5th conference, Gatlinburg 1995, pp. 341–347.

Rosen, P.A., Hensley, S., Joughin, I.R., Li, F.K., Madsen, S.N., Rodriguez, E., Goldstein, R.M. (2000) 'Synthetic aperture radar interferometry', Proceedings of the IEEE, 88(3), pp. 333–382. https://doi.org/10.1109/5.838084

Sadek, M. and Shahrour, I. (2004) 'A three dimensional embedded beam element for reinforced geomaterials', International Journal for Numerical and Analytical Methods in Geomechanics. John Wiley & Sons, Ltd, 28(9), pp. 931–946. https://doi.org/10.1002/nag.357

SA Sarmap. Sarscape® user guide. Harris Geospatial. Available at: https://www. harrisgeospatial.com/docs/pdf/sarscape 5. 1 help. pdf, 2014.

Schanz, T. and Vermeer, P. A. (1996) 'Angles of friction and dilatancy of sand', Géotechnique, 46(1), pp. 145–151. https://doi.org/10.1680/geot.1996.46.1.145

Selvakumaran, S., Rossi, C., Marinoni, A., Webb, G. Bennetts, J., Barton, E., Plank, S. and Middleton, C.. (2020) Combined InSAR and terrestrial structural monitoring of bridges. IEEE Transactions on Geoscience and Remote Sensing, 58(10):7141–7153. https://doi.org/10.1109/TGRS.2020.2979961

Selvakumaran, S. (2020). Interferometric Synthetic Aperture Radar for remote satellite monitoring of bridges. PhD thesis, University of Cambridge, Cambridge, UK. Https://doi.org/10.17863/CAM.51027

SMARTEC (2010) DiTeSt Reading Unit: high accuracy and long range distributed strain and temperature sensing system (BOTDA).

Sparrevik, P., Meland, H. J. and Joonsang, P. (2022) 'Distributed fibre optic ground deformation sensing', in 11th International Symposium on Field Monitoring in Geomechanics (ISFMG2022).

Stanier, S.A., Blaber, J., Take, W.A. and White, D.J.. (2016) 'Improved image-based deformation measurement for geotechnical applications', Canadian Geotechnical Journal. NRC Research Press, 53(5), pp. 727–739. https://doi.org/10.1139/cgj-2015-0253

Tufano, R., Guerriero, L., Annibali Corona, M., Bausilio, G., Di Martire, D., Nisio, S., Calcaterra, D. (2022) Anthropogenic sinkholes of the city of Naples, Italy:an update. Nat Hazards 112, 2577–2608 . https://doi.org/10.1007/s11069-022-05279-x

Vorster, E. T., Klar, A., Soga, K., Mair, R.J.(2005) 'Estimating the Effects of Tunneling on Existing Pipelines', Journal of Geotechnical and Geoenvironmental Engineering. American Society of Civil Engineers, 131(11), pp. 1399–1410. https://doi.org/10.1061/(ASCE)1090-0241(2005)131:11(1399) .

Warner, J. (2004) Practical Handbook of Grouting. John Wiley & Sons.

Wille, M., Clauss, K., Valgur, M., Blüthgen, J., Sølvsteen, J., and Delucchi. L.(2017). Sentinelsat (v0.12): Utility to search and download copernicus sentinel satellite images., https://doi.org/10.5281/zenodo.841118

Xu, X., Abadie, C. N., Möller, T., Della Ragione, G. & da Silva-Burke, T.S. (2022a) 'On the use of high-resolution distributed fibre optic sensing for small-scale geotechnical experiments at 1g', in 10th International Conference on Physical Modelling in Geotechnics (ICPMG). Daejeon, Korea.

Xu, X., Kechavarzi, C., de Battista, N., Hangen, H., Wright, D. (2022b) 'Fibre optic instrumented geogrid for ground movement detection', in 11th International Symposium on Field Monitoring in Geomechanics (ISFMG2022)

Yang, K., Yan, L., Huang, G., Chen, C., and Wu. (2016) Monitoring building deformation with insar: Experiments and validation. Sensors, 16(12):2182, https://doi.org/10.3390/s16122182

Zhao, Y., Gafar, K., Elshafie, M.Z.E.B., Deeks, A.D., Knappett, J.A. & Madabhushi, S.P.G. (2006) 'Calibration and use of a new automatic sand pourer', in Physical Modelling in Geotechnics, 6th ICPMG'06 - Proceedings of the 6th International Conference on Physical Modelling in Geotechnics, pp. 265–270.